Chapter 9

Investigation of Organic Bulk Heterojunction Solar Cells from Optical Aspect

Chunfu Zhang, Yue Hao, Dazheng Chen,
Zhizhe Wang and Zhenhua Lin

Additional information is available at the end of the chapter

http://dx.doi.org/10.5772/52819

1. Introduction

Low in cost, light in weight and flexible in mechanics, the solution-processed organic solar cells have aroused worldwide interest and have been the promising alternative to the traditional silicon-based solar cells [1-4]. However, they are still not available for the commercialization due to their low power conversion efficiency (PCE). Therefore, many research works have focused on the employing of new materials and device structures to improve the device performance. The milestone is the introduction and application of the bulk heterojunction structure consisting of an interpenetrating network of electron donor and acceptor materials [5]. By using this structure, the conventional organic solar cell (OSC) with poly(3-hexylthiophene)/[6,6]-phenyl C61-butyric acid methyl ester (P3HT:PCBM) blend shows a superior performance. Recently, the inverted organic solar cell (IOSC, in which the polarities of the two electrodes are exchanged) has also been introduced as the possible candidate for OSC to remedy the low air stability of OSC [6]. Both OSC and IOSC are now attracting the research interest. However, most of the previous works are mainly done for OSC or IOSC separately, and almost no researches are reported about the systemic comparison between OSC and IOSC for their different performances besides the air stability. Since the reported PCE of IOSC is relatively lower than that of OSC in many researches, one may doubt that which structure is better, the conventional one or the inverted one? As a result, one section of this chapter aims to investigate the performance differences of OSC and IOSC.

Although PCE of the standalone organic solar cell (including OSC and IOSC) is improved continuously with the research development, some bottlenecks still seem to appear because of the drawbacks coming from the molecular and macromolecular materials: First, the organic solar cell is dominated by the excitonic effect, the relatively short lifetime and the low

charge mobility, and these factors limit the maximum thickness of the active layer for light absorption. Second, most organic semiconducting materials show discrete absorption behaviour and cover only a fraction of the solar spectrum, leading to inefficient light harvest. To overcome these drawbacks, the realization of the tandem structure based on complementary thin absorber materials provides a reasonable solution to the above obstacles. As a promising concept to achieve high PCE, the tandem solar cell can reduce the loss via subbandgap transmission of photons, the major loss mechanism in solar cells [7]. For an ideal tandem solar cell, it requires current matching of the subcells, a lossless recombination contact and a complementary absorption of the subcells. Among them, current matching of the subcells is a leading design criterion for improving the tandem device performance. Then, the organic tandem solar cell optimization by considering the current matching is also involved in this chapter.

As is well known, the working principle of organic photovoltaic devices can be simply described as a process of "light in- current out". This process consists of seven parts:

1. in-coupling of photon,

2. photon absorption,

3. exciton formation,

4. exciton migration,

5. exciton dissociation,

6. charge transport, and

7. charge collection at the electrodes.

The first two parts are the optical mechanisms of the device and the other parts constitute the electrical aspect. The optical aspect plays a significant role because more incident photons and absorbed photons are the baseline for the better device performance. It has been reported that the internal quantum efficiency (IQE) of organic bulk heterojunction solar cells can reach 100% [8]. Thus the external quantum efficiency (EQE) can be approximately described as the product of IQE and the ratio of the number of absorbed photons in active layer to the number of incoming photons. As a result, the optimization of organic solar cells from the optical aspect is seriously important. This is why we investigate the device performance of standalone and tandem organic solar cells mainly from the optical aspect in this work.

The contents of this chapter are arranged as the following: Section 2 investigates the performance of the standalone conventional and inverted organic solar cells, especially the performance differences between the two types of devices. Section 3 discusses the optimization of the organic tandem solar cell from the optical aspect by considering the current matching. At last, a short conclusion is given in Section 4.

http://dx.doi.org/10.5772/52819

2. Invetigation of Standalone Organic Solar Cells

2.1. Methology

In order to investigate the standalone organic solar cell, we have performed optical simulations based on the Transfer Matrix Formalism with two subsets of 2×2 matrices (layer matrix and interface matrix), which was firstly introduced into organic solar cells by Pettersson et al [9] and now has been used widely. In this method, the cell is treated as a one-dimensional stack of homogeneous and isotropic layers with flat interfaces, and the number of photons absorbed in the active layer is obtained by calculating the time average of the energy dissipated per second in it. The detailed calculation processes are not presented here since the transfer matrix method is widely applied [10].

In the calculation, we assume that one absorbed photon produces one exciton in the active layer and one exciton divides into two free charges (one electron and one hole), and one electron (or hole) is collected by cathode (or anode). As a result, the number of photons absorbed in the active layer can be used as the substitute for the maximum possible short circuit current density and the EQE can be simplified as the ratio of the number of photons absorbed in the active layer to the number of incident photons.

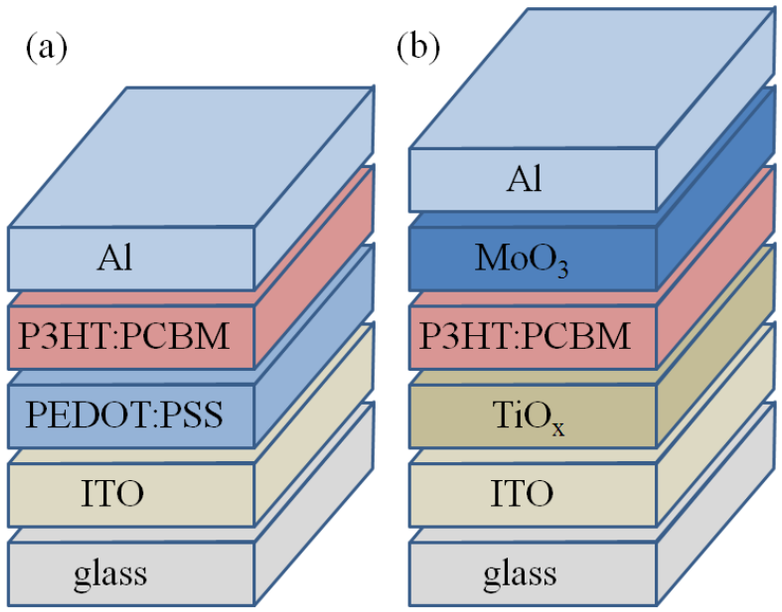

Figure 1. Schematic illustration of the conventional organic solar cell (OSC) with a structure of ITO/PEDOT:PSS/P3HT:PCBM/Al (a), and the inverted organic solar cell (IOSC) with a structure of ITO/TiO_x/P3HT:PCBM/MoO_3/Al (b). For OSC, the layers of ITO/PEDOT:PSS act as anode and Al acts as cathode, however for ISOC, the layers of TiO_x/ITO and Al play the roles of cathode and anode, respectively. Meanwhile, the layers of TiO_x and MoO_3 are chosen for electron and hole transport layers. The P3HT:PCBM (1:1) is the active layer and the incident light enters devices from glass in both structures.

In this optical model, the layer of P3TH:PCBM is chosen as the active layer. OSC has the structure of ITO (150 nm)/PEDOT:PSS(50 nm)/P3HT:PCBM(x nm)/Al(100 nm) and ISOC has

the structure of ITO(150 nm)/TiO_x (10 nm)/P3HT:PCBM(x nm)/MoO_3 (10 nm)/Al (100 nm), as shown in Fig.1. The optical constants of P3HT:PCBM, PEDOT:PSS, ITO, TiO_x, MoO_3, ZnO and Al are obtained from literatures [11-13].

It should be noted that, the reflection of the glass substrate is taken into account to revise the initial intensity of optical electric field at glass/ITO interface and can be described as

$$|E_{0g}|^2 = \frac{1-R^*}{n_g(1-RR^*)}|E_0|^2 \quad (1)$$

where R* represents the reflectance of air/glass interface, R the reflectance for the stack structure, n_g the refraction coefficient of glass and $|E_0|^2$ (modulus squared of the optical electric filed) the initial intensity of optical electric field when light arrives at air/glass interface.

To calculate the number of absorbed photons (or excitons) in the active layer, the energy flow dissipation per second for single wavelength in active layer, Q is given as

$$Q = \frac{1}{2}c\varepsilon_0\alpha n|E|^2 \quad (2)$$

where c is the speed of light, ε_0 the permittivity of vacuum, α the absorption coefficient, n the real index of refraction, and $|E|^2$ the total optical electric field intensity in the multilayer stack at single wavelength. Then the number of photons absorbed in the active layer can be expressed as

$$N = \int_{\lambda=300nm}^{800nm} Q(\lambda)\frac{\lambda}{hc}d\lambda \quad (3)$$

where N represents the number of photons absorbed in the active layer, hc/λ the photon energy at a specified wavelength λ, h the Planck constant and c the speed of light. The devices are illuminated with AM 1.5G solar spectra.

2.2 Results and discussion

The number of photons absorbed in the active layer as a function of the active layer thickness is obtained for OSC and IOSC, as well the EQE as a function of the wavelength or the active layer thickness. The optical modulation effect is investigated by inserting a ZnO layer between P3HT: PCBM and Al for OSC, and changing the thickness of MoO_3 layer for ISOC, respectively.

http://dx.doi.org/10.5772/52819

Comparison of photons absorbed in the active layer

The results of the number of photons absorbed in the active layer as a function of the active layer thickness for OSC are shown in Fig. 2(a). It is clear that the number of absorbed photons increases with the active layer thickness and one can see a notable behavior of oscillation which is due to the optical interference effect induced by the incident light and the reflected light from the mirror metal electrode. The inserting of a ZnO layer leads to the shift of interference maxima to lower thicknesses and the remarkable increase of absorbed photons especially for the relatively thin active layer. However, the insertion of a ZnO layer makes no improvement near the active layer thicknesses where the interference maxima are obtained. This variation of the number of absorbed photons with the active layer thickness is the same as that of maximum possible short circuit current density in other researches [14].

For IOSC, Fig. 2(b) shows the same tendency as OSC. It is obvious that the influence of optical modulation effect is more slightly when the active layer is relatively thick (about 150 nm). Comparing OSC with IOSC, as shown in Fig. 2 (c), it is clear that the number of absorbed photons in IOSC is larger at any active layer thicknesses except for the thicknesses around which the interference maxima of OSC are obtained. In other words, for most active layer thicknesses, the light absorption in IOSC is more effective, hence the larger contribution to photocurrent. It has been reported that the refractive index of TiO_x is very similar to that of PEDOT:PSS, therefore the light loss induced by the reflection at the ITO/TiO_x interface and that at the ITO/PEDOT:PSS interface is nearly equivalent. However, light absorption loss in the TiOx layer is smaller than that in the PEDOT:PSS layer [15].In addition, the layer of MoO_3 in IOSC can act as an optical spacer layer. As a result, one can say the better light absorption in IOSC is attributed to the nearly equal amount of entering light and the smaller absorption loss in TiO_x layer, as well as the optical modulation effect caused by MoO_3 layer. Although IOSC shows a better performance than OSC at most of the active layer thicknesses, it is noted that the performance of IOSC is slightly lower than that of OSC around the interference peaks as shown in Fig. 2(c). One possible reason is the parasitic absorption in the MoO_3 layer, because not only the the optical modulation effect but also the absorption loss could be caused by the MoO_3 layer, which produces a tradeoff.

To well understand the difference between OSC and IOSC, the distribution of optical electric field is investigated at different active layer thicknesses. According to the absorption coefficient of P3HT:PCBM calculated by $\alpha=4\pi k/\lambda$, the maximum absorption coefficient is obtained at the incident light wavelength of around 512 nm, which agrees to the range of maximum absorption coefficient from 500 nm to 550 nm for P3HT:PCBM active material. As a result, the incident light of 512 nm is chosen to calculate the optical electric field distribution. The distributions of normalized modulus squared optical electric field at three different active layer thicknesses (45, 85, and 150 nm) for OSC and IOSC are shown in Fig. 3. The thickness of TiO_x is specified as 50 nm to make the active layer region at same position in Fig. 3 for a clear comparison since its thickness has no significant influence on the photons absorbed in the active layer. Fig. 3(a) and (c) illustrate that the area below the curve of IOSC is larger than that below the curve of OSC for both thin and thick devices, which is consistent with the more absorbed photons in IOSC. And from Fig. 3(b), the opposite result can be seen when the

active layer is 85 nm where the interference maximum of OSC is obtained, which agrees to the situation in Fig. 2(c). The similar results will also be shown in next part where the different performances of EQE for OSC and IOSC are discussed.

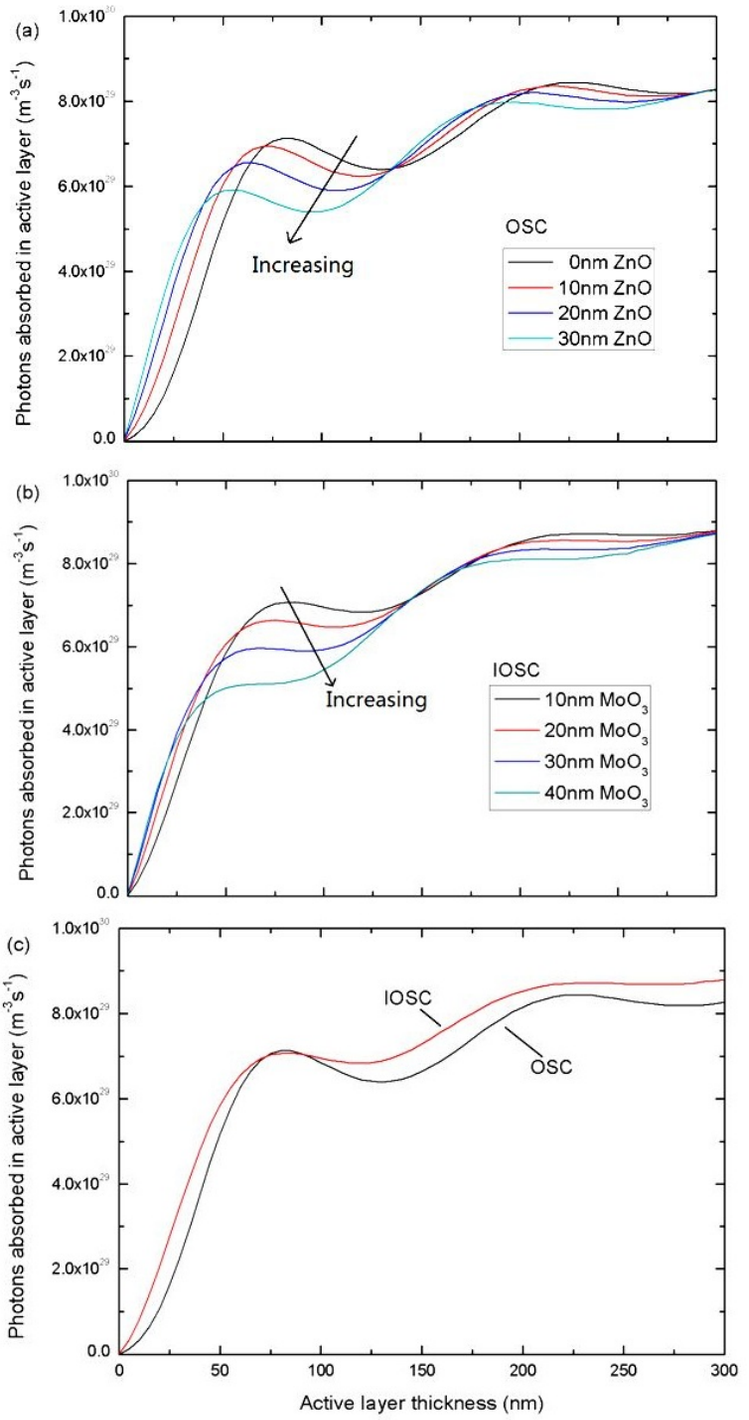

Figure 2. Number of photons absorbed in the active layer versus the active layer thickness with various thicknesses of the optical spacer layer. (a) OSC with the ZnO layer thickness ranging from 0 to 30 nm. (b) IOSC with the MoO_3 layer

http://dx.doi.org/10.5772/52819

thickness ranging from 10 to 40 nm. (c) Comparison of the number of photons absorbed in active layer of OSC and ISOC as a function of the active layer thickness. In this case, no ZnO layer is inserted in OSC and the thickness of MoO_3 is specified as 10 nm for ISOC.

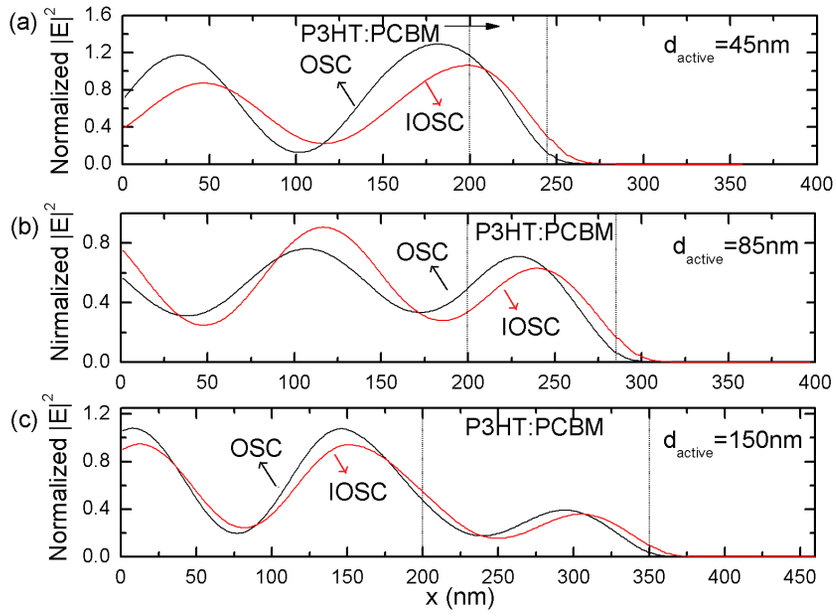

Figure 3. Normalized optical electric field distribution varies with the distance from glass/ITO interface for OSC (black) and IOSC (red) devices. The incident light wavelength is specified as 512 nm. The active layer thicknesses are 45 nm (a), 85 nm (b), and 150 nm (c), respectively.

Comparison of EQE

The EQE as a function of incident light wavelength for OSC and IOSC is shown in Fig. 4, and the thicknesses of the active layer are specified as 40, 80, 160 and 220 nm. For OSC in Fig. 4(a), the EQE trends to increase with the thickness of the P3HT:PCBM layer in the range of wavelength from 450 to 650 nm. It should be noted that, the lower EQE at 160 nm than 80 nm can be explained by the fact that 80 nm is closed to the thickness where the first interference maximum of OSC is obtained (Fig. 2(c)). At the same time, the wavelength range possessing higher EQE is also expanded especially at the wavelength near 600 nm, where the shoulders are generally changed into peaks with the increasing of the active layer thickness. Of course, for the light over 650 nm, it prefers thicker active layer to achieve better absorption of light, and for the light near 400 nm, the variation of EQE with the active layer thickness displays a behavior of increase and decrease in turn. The similar results can be obtained from Fig.4 (b) for IOSC. For the thicker active layer beyond 220 nm, the same simulation results can be obtained (not presented here) and the results are agreed to the measured EQE of OSC and IOSC with 250 nm thick active layer. In short, the thick active layer brings higher EQE for both OSC and IOSC, and the main absorption range from 400 to 650 nm can be observed from Fig. 4.

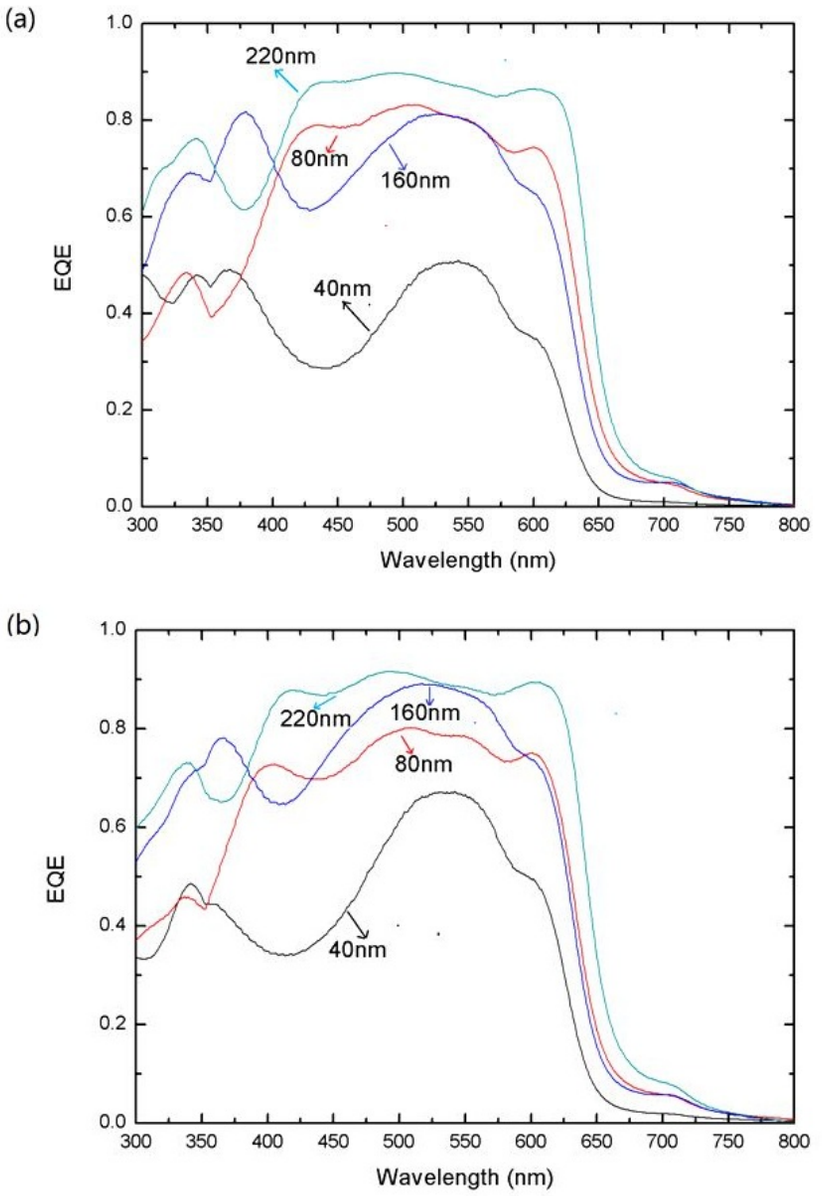

Figure 4. EQE vs. wavelength for OSC (a) and IOSC (b) with four different thicknesses of active layer: 40 nm(black), 80 nm(red), 160 nm(blue), and 220 nm(green), respectively.

The comparison of EQE varying with the wavelength for OSC and IOSC is presented in Fig. 5. It is evident that IOSC with 40 and 160 nm active layer has better performance in EQE in the main absorption range. However, for the 80 and 220 nm active layer, the EQE of OSC is closed to or even higher than that of IOSC, which is due to the fact that these two thicknesses nearly equal the thicknesses where the interference maxima of OSC are obtained. In other words, IOSC is super to OSC in EQE in the main absorption range for both thin and thick active layers except for thicknesses around which the interference maxima of OSC are obtained, which agrees to the analysis of the number of photons absorbed in active layer in Fig. 2. Hence the explanation is the same for this result.

http://dx.doi.org/10.5772/52819

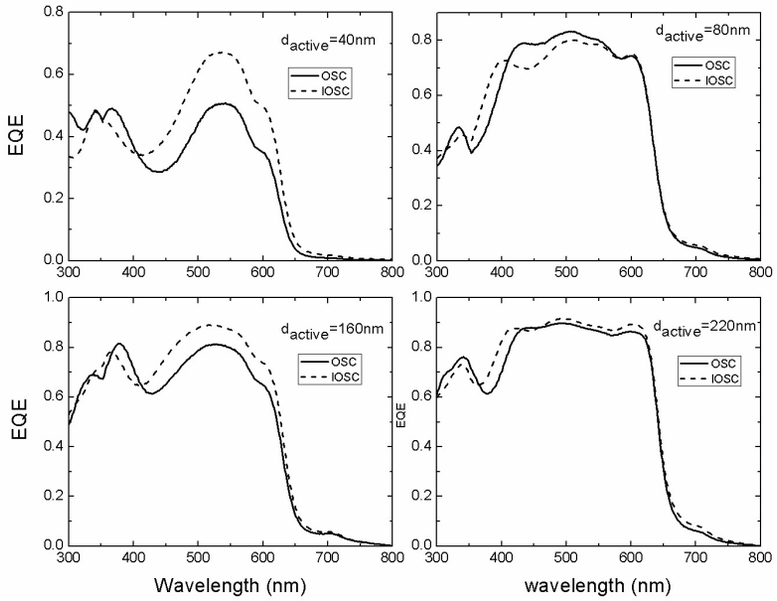

Figure 5. Comparison of EQE as a function of wavelength for OSC (solid line) and IOSC (dash line) with four different active layer thicknesses: 40 nm, 80 nm, 160 nm, and 220 nm.

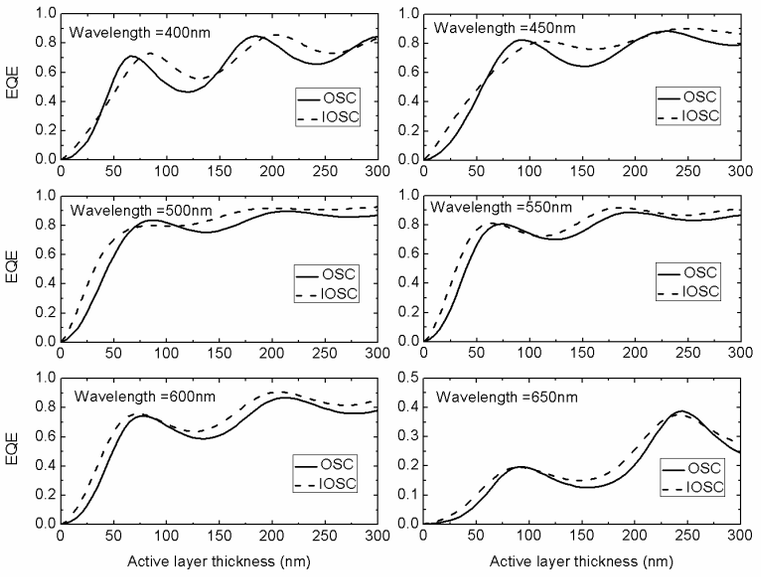

Figure 6. Comparison of EQE as a function of the active layer thickness for OSC (solid line) and IOSC (dash line) with six wavelengths of incident light: 400 nm, 450 nm, 500 nm, 550 nm, 600 nm, and 650 nm.

Light wavelength (nm)		400	450	500	550	600	650
OSC	Position (nm)	65	95	85	75	75	90
	EQE	0.7100	0.8252	0.8363	0.8060	0.7437	0.1975
IOSC	Position (nm)	85	115	85	65	75	90
	EQE	0.7306	0.8150	0.7987	0.8109	0.7574	0.1952

Table 1. The positions and amplitudes of the first maximum EQE of OSC and IOSC at different wavelengths. The positions correspond to the active layer thickness and OSC behaves slighter thickness oscillation behavior than IOSC.

To verify the above conclusion, the EQE as a function of the active layer thickness at different wavelengths of incident light is investigated. For the EQE of OSC and IOSC depicted in Fig. 6, a remarkable increase and oscillation behavior with the increase of the active layer thickness can be observed. From Fig. 6, a conclusion may be obtained that IOSC performs better than OSC at any thickness of active layer for the light ranging from 400 to 650 nm. However, at the active layer thicknesses around which the interference maxima of OSC are obtained, the EQE of OSC is close to or even higher than that of IOSC. To well investigate the difference between OSC and IOSC, the positions and amplitudes of the first maximum EQE at different wavelengths are shown in Table 1. The clear oscillation behavior of the positions and amplitudes of the maximum EQE can be seen for both OSC and IOSC, and OSC exhibits more slight thickness oscillation behavior than IOSC. It is evident that the slight oscillation of maxima at single wavelength is beneficial to the final maximum in the range including all wavelengths. Therefore, the results from Table 1 can also be used to explain the results shown in Fig. 2(c) and Fig. 5.

In summary, from pure optical aspect, OSC and IOSC have the same tendency in the number of photons absorbed in the active layer, EQE, and the optical electric field distribution as well as the similar influence of optical modulation effect. However, IOSC performs better than OSC except for the case wherein the interference maxima of OSC are obtained, which is due to the better light absorption of ISOC possible absorption loss caused by MoO3 layer.

3. Investigation of the Organic Tandem Solar Cell

Although PCE of the organic solar cell is improved continuously, there are still some drawbacks for standalone devices: First, the organic solar cell is dominated by the excitonic effect, the relatively short lifetime and the low charge mobility. All of these limit the maximum thickness of the active layer for light absorption. Second, most organic semiconducting materials show discrete absorption behavior and cover only a fraction of the solar spectrum, leading to inefficient light harvest. The realization of the organic tandem solar cell based on complementary thin absorber materials provides a reasonable solution to improve device performance further.

In the existing views, matching the photocurrents of the subcells leads to the maximum PCE in the corresponding tandem cell, making it a crucial design criterion for optimum perform-

http://dx.doi.org/10.5772/52819

ance. Then to achieve a better device performance, the tandem cell should be optimized by considering current matching.

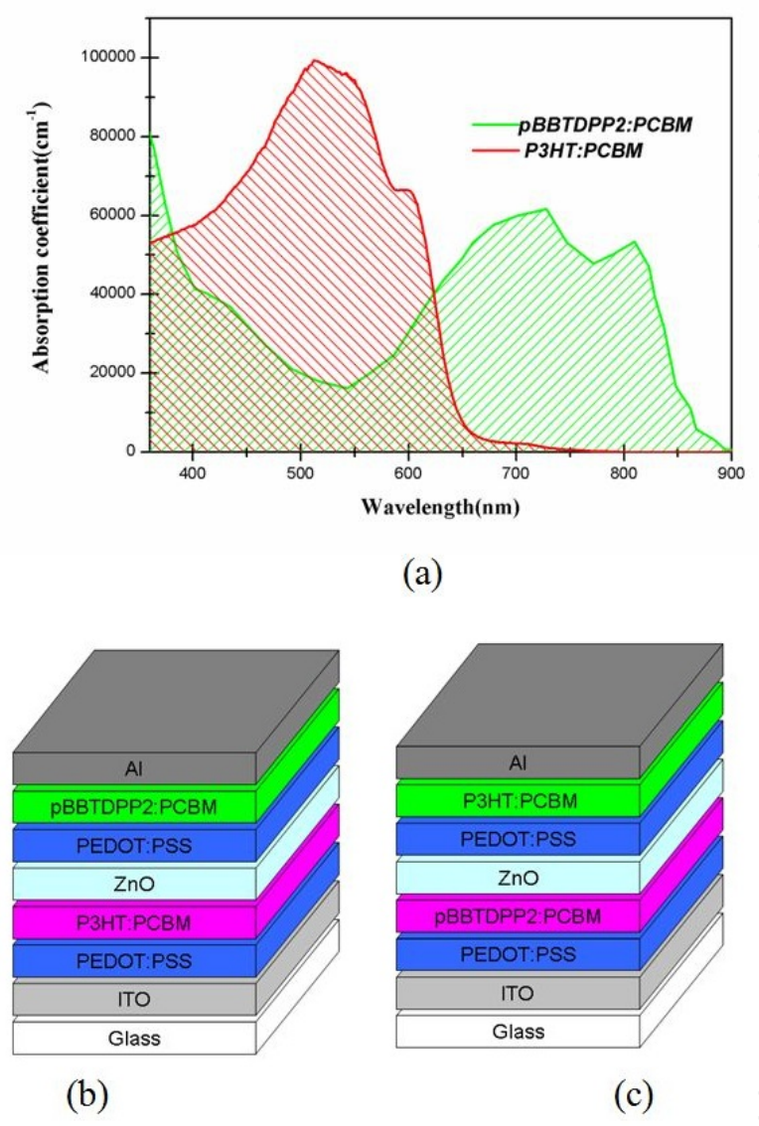

Figure 7. a) Absorption coefficients of both individual active layers. b) Normal and c) Reversed device structure.

As discussed in previous section, P3HT has been widely used as the donor conjugated polymer in the quest for high-efficiency bulk heterojunction organic solar cells. Its combination with PCBM as the acceptor is a standard active layer of organic solar cells based on polymer, whereas the low-energy onset of the absorption of this combination at about 650 nm limits the number of photons absorbed in the active layer. Recently, a very promising organic material has been reported and applied [16], namely poly[3,6-bis-(40-dodecyl-[2,20] bithiophenyl-5-yl)-2,5-bis-(2-ethyl-hexyl)-2,5-dihydropyrrolo[3,4-]pyrrole-1,4-dione] (pBBTDPP2). This new polymer combines electron-rich quaterthiophene (BBT) segments with electron-poor diketo pyrrolo-pyrrole (DPP) units to lower the optical bandgap to 1.4 eV in thin films. The onset of

the absorption of the blend of pBBTDPP2 and PCBM is significantly shifted to 860 nm with o-dichlorobenzene as solvent. Thus, a series connected tandem solar cell based on P3HT:PCBM and pBBTDPP2:PCBM almost covers the whole UV and visible parts of the solar spectrum, making it attractive (see Fig. 7 (a)). It is necessary to carefully optimize the thicknesses of the front and back cells for different layer sequences to deeply exploit the opportunity provided by this tandem solar cell. Therefore, detailed optical simulations of tandem cells based on P3HT:PCBM and pBBTDPP2:PCBM have been carried out in this chapter.

3.1. Methodology

As in previous section, the calculation is still based on the Transfer Matrix Formalism. The basic structure of the tandem solar cell is shown in Fig. 7(b). On top of the glass, a 100 nm indium-tin-oxide (ITO) layer is used as the anode, followed by a 50 nm layer of PEDOT:PSS and a front active layer with variable thicknesses. The recombination contact consists of a 30 nm ZnO layer and a 15 nm PEDOT:PSS layer, followed by a back active layer with variable thicknesses. Finally, 100 nm Al is deposited to realize the cathode. In conventional tandem solar cells, materials mainly absorbing light of shorter wavelengths act as the front active layer to provide a window for the back cell while materials mostly absorbing light of longer wavelengths work as the back active layer. Thus the device with P3HT:PCBM in the front cell and pBBTDPP2:PCBM in the back cell is defined as“Normal Tandem Solar Cell” or “NTSC”, the device with pBBTDPP2:PCBM in the front cell and P3HT:PCBM in the back cell as “Reverse Tandem Solar Cell” or “RTSC”.

Before starting our work, three assumptions should be stated. First, an electron-hole pair is generated in the solar cell with every photon absorbed. Second, Ohmic losses in the recombination contact and the spacer are negligible. In consequence, the open circuit voltage of the tandem solar cell is a summation of those of both subcells. Thus, the performance of the tandem solar cell is mainly determined by its short circuit current density (J_{SC}). Three, the glass substrate is thicker than the coherence length of light, so optical interference in it can be neglected.

The optical parameters (n and k) of P3HT:PCBM (1:1 in weight), pBBTDPP2:PCBM (1:2 in weight), ITO, ZnO, PEDOT:PSS and Al used in this work are obtained from literatures [11, 14, 17, 18].

Considering current matching, we optimize the thicknesses of the front and back cells for NTSC and RTSC respectively. All the calculations are carried out under AM 1.5G radiation.

3.2. Results and discussion

According to the existing views, the optimized PCE can be obtained when the photocurrents of the subcells are matched. Thus, we vary the thicknesses of both the front (d_{front} between 10 and 250 nm) and back (d_{back} between 10 and 200 nm) active layers to investigate J_{SC} of both subcells.

http://dx.doi.org/10.5772/52819

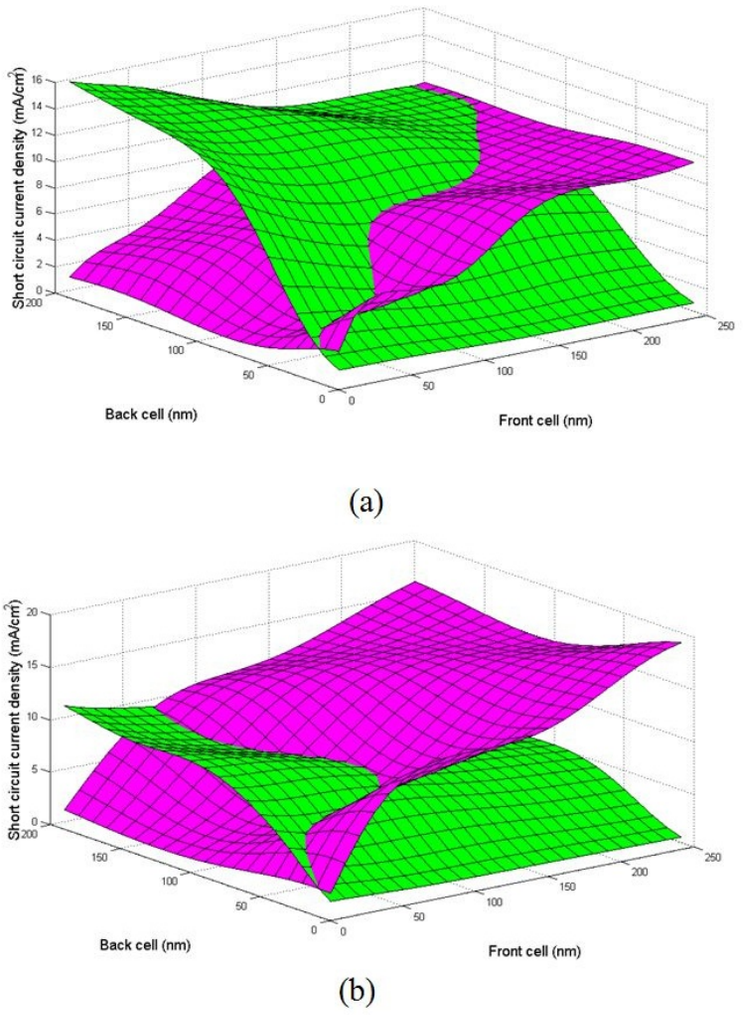

Figure 8. a) and b) 3D plots of $J_{SC(front)}$ (magenta) and $J_{SC(back)}$ (green) versus d_{front} and d_{back} for NTSC and RTSC.

Such a result of the calculation is plotted in Figs. 8 (a) and (b) for NTSC and RTSC separately. J_{SC} for the front ($J_{SC(front)}$) and back ($J_{SC(back)}$) cells are shown in the three-dimensional (3D) space as surfaces, magenta and green, respectively. Figures 9 (a) and (b) display the same results as Figs. 8 (a) and (b) respectively, but in a two-dimensional format. In NTSC, the front cell may provide up to a J_{SC} of 11.22 mA/cm^2 when d_{back}=10 nm. Whereas when d_{back} increases up to 200 nm, $J_{SC(front)}$ can decrease down to 10.30 mA/cm^2. Because the front cell is much far from the mirror Al electrode, $J_{SC(front)}$ scarcely shows any interference oscillation in the variation range of d_{back}. Thus, this 8% loss is $J_{SC(front)}$ not induced by the interference effect but the reduction of the amount of light reflected from the Al surface (and arriving at the front cell a second time) as the thickness of the back cell increases. The variation of $J_{SC(back)}$ is more strongly affected by d_{front} than vice versa. While for d_{front}=10 nm, $J_{SC(back)}$ goes up to 15.76 mA/cm^2. However, when d_{front}=250 nm, $J_{SC(back)}$ reduces to 10.29 mA/cm^2. This is obviously caused by the absorption spectra overlap of the two active layer materials (see Fig. 7(a)), which reduces photons arriving at the back cell. Because the back cell is much nearer to the Al electrode than the front cell, the interference behavior of $J_{SC(back)}$ is very obvious as

shown in Fig. 9(a). Because of the same reason, the same tendency can be observed in RTSC (see Figs. 8(b) and 9(b)). In RTSC, while for d_{back}=10 and 200 nm, $J_{SC(front)}$ goes up to 18.93 and 16.04 mA/cm^2, respectively. With the increase of d_{front} from 10 to 250 nm, $J_{SC(back)}$ decreases from 10.97 to 5.53 mA/cm^2. A obvious increase of J_{SC} of pBBTDPP2:PCBM layer and a strong decrease of J_{SC} of P3HT:PCBM layer can be observed in RTSC, compared with NTSC. This is caused by the absorption difference of two blends. As shown in Fig. 7(a), the spectral range of pBBTDPP2:PCBM is much wider than that of P3HT:PCBM (the former absorbs photons in the nearly entire wavelength range discussed while the latter hardly absorbs photons of wavelengths beyond 650 nm). Therefore, when acting as the front active layer, pBBTDPP2:PCBM hinders the harvest of photons in P3HT:PCBM more strongly than that in P3HT:PCBM with pBBTDPP2:PCBM as the back active layer.

NTSC				RTSC				difference
d_{front}	d_{back}	$J_{sc(front)}$	$J_{sc(back)}$	d_{front}	d_{back}	$J_{sc(front)}$	$J_{sc(back)}$	Δ
6	10	1.00	0.89	7	10	1.06	1.09	-0.20
8	20	1.55	1.55	11	20	2.17	2.09	-0.53
15	30	2.64	2.57	15	30	3.18	3.29	-0.71
58	40	3.28	3.26	21	40	4.26	4.35	-1.09
73	50	4.20	4.14	32	50	5.25	5.17	-1.04
80	60	5.21	5.22	66	60	6.05	6.06	-0.84
87	70	6.32	6.35	102	70	6.75	6.73	-0.37
99	80	7.49	7.46	109	80	7.12	7.12	0.34
173	90	8.76	8.77	110	90	7.42	7.38	1.39
191	100	9.28	9.29	107	100	7.54	7.53	1.76
201	110	9.55	9.57	102	110	7.59	7.59	1.98
210	120	9.72	9.70	96	120	7.62	7.58	2.12
218	130	9.81	9.80	89	130	7.58	7.57	2.24
228	140	9.93	9.92	82	140	7.54	7.60	2.32
238	150	10.09	10.09	77	150	7.73	7.70	2.39
245	160	10.24	10.23	72	160	7.86	7.92	2.30
247	170	10.29	10.29	70	170	8.26	8.21	2.08
246	180	10.28	10.28	68	180	8.51	8.57	1.71
245	190	10.25	10.25	69	190	8.90	8.90	1.34
244	200	10.21	10.20	72	200	9.18	9.16	1.04

Table 2. Current matching points for NTSC and RTSC, corresponding to the black dots of the bold lines in Figs. 9 (a) and (b) respectively. Corresponding $J_{SC(front)}$, $J_{SC(back)}$, d_{back} and d_{front} are all displayed here. The differences between matching J_{SC} of NTSC and RTSC displayed in the same row are shown in the last column (Δ). d is in nm and J_{SC} is in mA/cm^2 here.

The bold lines in Figs. 9 (a) and (b) represent the intersection between both surfaces in the corresponding 3D plots, namely, current matching points of the subcells, which correspond

http://dx.doi.org/10.5772/52819

to the optimized thicknesses of the active layers. Seen from Figs. 9(a) and (b), it is obvious that a single value for d_{front} can have more than one counterpart d_{back} along the bold line for RTSC while there is only one counterpart d_{back} for NTSC. This interesting thing leads us to list the optimized active layer thicknesses in Table 2 for NTSC and RTSC, respectively. It can be observed from Table 2 that RTSC shows its superiority in matching J_{SC} when the active layers of both subcells are relatively thin. We note that RTSC can provides a larger matching J_{SC} with a smaller d_{front} when the device is relatively thin (d_{back} is usually less than 100 nm). But NTSC is better as the thicknesses of both active layers increase, in agreement with the general view presented.

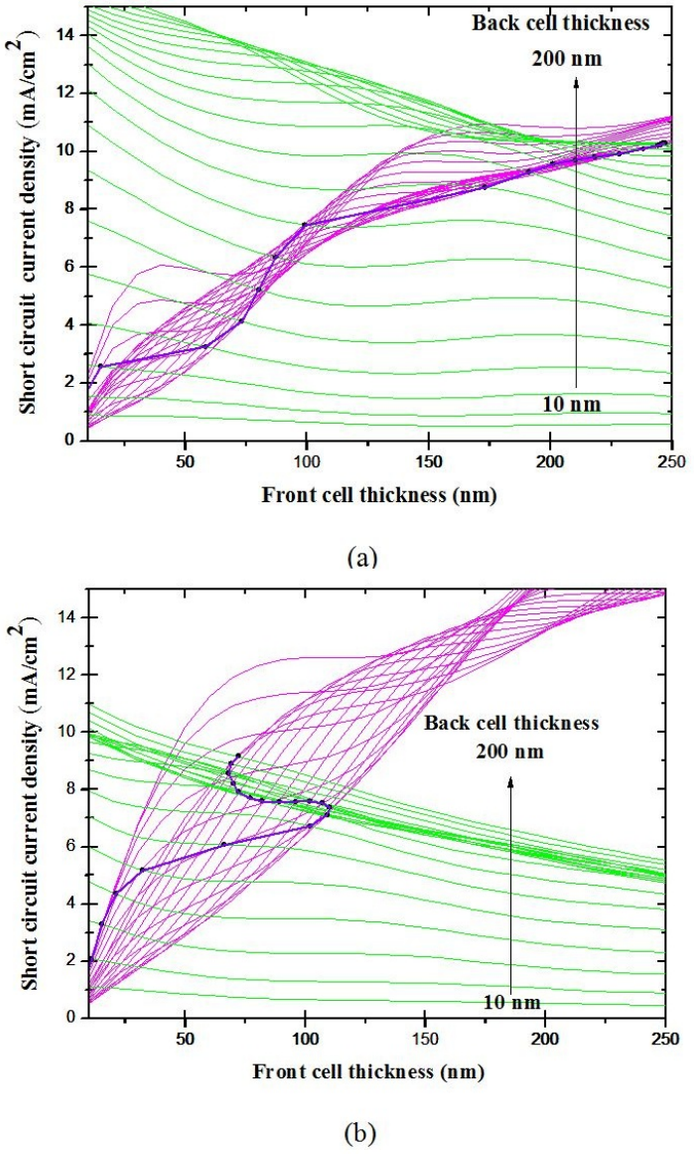

Figure 9. a) and b) Different viewing angle of the 3D plots shown in Figs. 8 (a) and (b), respectively. Every magenta or green line indicates $J_{SC(front)}$ or $J_{SC(back)}$ versus d_{front} with the fixed d_{back}. d_{back} is ranging from 10 to 200 nm in a uniform step of 10 nm (see the arrow).

In order to well understand this amazing phenomenon, optical electric field distributions of tandem solar cells should be taken into account. Four current matching points listed in Table 2 are used here: a 58-40-nm NTSC, a 21-40-nm RTSC, a 238-150-nm NTSC and a 77-150-nm RTSC. The reason why we choose these points is that the matching J_{SC} differences between the corresponding NTSC and RTSC reach the maxima in positive and negative, respectively (see Δ, the last column in Table 2). The distributions of normalized modulus squared of optical electric filed $|E|^2$ for the above tandem solar cells are calculated and shown in Fig. 10 (the shadow area indicates the active layers of the front (left) and back (right) cells). As shown in Fig. 7(a), 512 and 600 nm are around the peak and shoulder of the absorption spectrum of P3HT:PCBM respectively while 727 and 809 nm are around two absorption maxima of pBBTDPP2:PCBM. Thus, the cases for wavelengths of 512, 600, 727 and 809 nm are discussed here. By observing optical electric filed distributions of a 58-40 nm NTSC and a 21-40-nm RTSC (both active layers are relatively thin) as shown in Figs. 10 (a) and (b), it is very clear that RTSC has a better optical electric filed distribution in both active layers although it has a smaller d_{front}, in accordance with the values of J_{SC} shown in Table 2. It can be explained by the properties of the materials and device structures. As shown in Figs. 10 (a) and (b), no matter with which structure, the peaks of optical electric field for light of wavelengths of 727 and 809 nm are usually near or in the front active layer. Since pBBTDPP2:PCBM mainly absorbs light of longer wavelengths and P3HT:PCBM absorbs light of shorter wavelengths, RTSC (place pBBTDPP2:PCBM in the front and P3HT:PCBM in the back) has a better performance when the active layers are thin. However, things become different when the device becomes thicker and thicker. For a very thick RTSC, the first interference peaks for wavelengths of 727 and 809 nm begin to leave the front active layer and then the pBBTDPP2:PCBM subcell is no longer an effective device. At the same time, owing to the much wider spectral range of pBBTDPP2:PCBM, it hinders the harvest of photons in P3HT:PCBM with pBBTDPP2:PCBM as the front active layer. Thus, when the active layers become thicker (d_{back} is usually over 100 nm), RTSC only allows a smaller matching J_{SC} with a smaller d_{front} compared with NTSC and NTSC shows its superiority. This is in good agreement with the results in Table 2.

In conclusion, it is observed that RTSC takes over the lead in matching J_{SC} when the active layers are relatively thin; but NTSC allows a larger matching J_{SC} as the active layers are relatively thick. The similar results are also found in the tandem solar cell based on P3HT:PC_{70}BM and PCPDTBT:PC_{60}BM [19]. The results are very interesting since we can choose the thinner RTSC to achieve matching J_{SC}, which can alleviate the carrier transport problem and save the material cost.

http://dx.doi.org/10.5772/52819

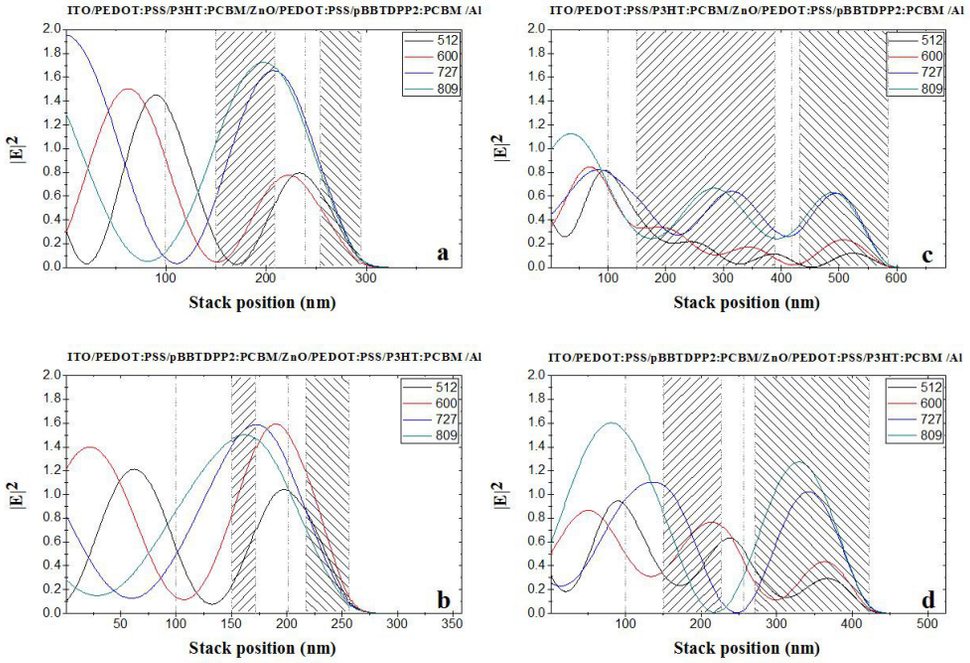

Figure 10. Calculated distributions of normalized modulus squared of optical electric field |E|2 inside a a) 58-40-nm NTSC b) 21-40-nm RTSC c) 238-150-nm NTSC d) 77-150-nm RTSC for four wavelengths of 512, 600, 727 and 809 nm.

4. Conclusion

The application of the bulk heterojunction structure consisting of an interpenetrating network of electron donor and acceptor materials greatly improves the standalone organic solar cells. Now there are mainly two types of standalone organic solar cells: OSC and IOSC. IOSC is introduced as the possible candidate for OSC to remedy the low air stability of OSC. However, most of the previous works reported that PCE of IOSC is relatively lower than that of OSC. As a result, the performance differences of OSC and IOSC are discussed in this work. It is concluded that in the optical aspect, OSC and IOSC have the same tendency in the number of photons absorbed in the active layer, EQE, and the optical electric field distribution as well as the similar influence of optical modulation effect. Normally, IOSC performs better due to the better light absorption of IOSC because the absorption loss in TiO_x layer for IOSC is smaller than that in PEDOT:PSS layer for OSC and the hole transporting layer (MoO_3 layer in this work) can play the role of optical layer. However, around the interference maxima of OSC, OSC shows better performance because the optical electric field has been optimized under this condition and there is no room for further improvement.

Although PCE of the standalone organic solar cell is improved continuously, there are still some drawbacks for this type of devices: First, the organic solar cell is dominated by the excitonic effect, the relatively short lifetime and the low carrier mobility. And these limit the maximum thickness of the active layer for light absorption. Second, most organic semiconducting materials show discrete absorption behavior and cover only a fraction of the solar

spectrum, leading to inefficient light harvest. The realization of organic tandem solar cells based on complementary thin absorber materials provides a reasonable solution to improve PCE further. In a tandem cell, to achieve the maximum PCE, it is necessary to ensure current matching of both subcells, which leads to detailed optical simulations in this work. At first, active layer thicknesses of the tandem cell are optimized by considering current matching for normal and reverse structures (see Fig. 7), respectively. Owing to the different spectral ranges of two blend materials (P3HT:PCBM and pBBTDPP2:PCBM) and device structures, it is noted that the reverse tandem cell allows a larger matching J_{SC} when the total device is relatively thin. When the thicknesses of the active layers increase, the normal tandem solar cell begins to present its superiority in the performance. This makes senses in the aspect of application that we can choose a thinner reverse tandem cell to achieve J_{SC} needed in some cases, which saves cost and increases the profit to an extent.

Acknowledgements

The work is supported by National Natural Science Foundation of China (61106063) and the Fundamental Research Funds for the Central Universities (K50511250003).

Author details

Chunfu Zhang[1*], Yue Hao[1*], Dazheng Chen[1], Zhizhe Wang[1*] and Zhenhua Lin[2]

*Address all correspondence to: cfzhang@xidian.edu.cn

1 School Of Microelectronics, Xidian University, China

2 ECE, National University of Singapore, Singapore

References

[1] Brabec, C. J., Sariciftci, N. S., & Hummelen, J. C. (2001). Plastic solar cells. *Adv. Funct. Mater*, 11(1), 15-26.

[2] Huynh, W. U., Dittmer, J. J., & Alivisatos, A. P. (2002). Hybrid nanorod-polymer solar cells. *Science*, 295(5564), 425-427.

[3] Kim, Y., Lee, K., Coates, N. E., Moses, D., Nguyen, T. Q., Dante, M., & Heeger, A. J. (2007). Efficient tandem polymer solar cells fabricated by all-solution processing. *Science*, 317(5835), 222-225.

[4] Zhang, C. F., Hao, Y., Tong, S. W., Lin, Z. H., Feng, Q., Kang, E. T., & Zhu, C. X. (2011). Effects of cathode confinement on the performance of polymer/fullerene photovoltaic cells in the thermal treatment. *IEEE Trans. Electron Devices*, 58(3), 835-842.

[5] Yu, G., Gao, J., Hummelen, J. C., Wudl, F., & Heeger, A. J. (1995). Polymer photovoltaic cells: enhanced efficiencies via a network of internal donor-acceptor heterojunctions. *Science*, 270(5243), 1789-1791.

[6] Pacios, R., Chatten, A. J., Kawano, K., Durrant, J. R., Bradley, D. D. C., & Nelson, J. (2006). Effects of photo-oxidation on the performance of poly [2-methoxy-5-(3′,7′-dimethyloctyloxy)-1, 4-phenylene vinylene]:[6,6]-phenyl C61-butyric acid methyl ester solar cells. *Adv. Funct. Mater*, 16(10), 2117-2126.

[7] Gregg, B. A., & Hanna, M. C. (2003). Comparing organic to inorganic photovoltaic cells: Theory, experiment, and simulation. *J. Appl. Phys*, 93(6), 3605-3614.

[8] Park, S. H., Roy, A., Beaupre, S., Cho, S., Coates, N., Moon, J. S., Moses, D., Leclerc, M., Lee, K., & Heeger, A. J. (2009). Bulk Heterojunction Solar Cells With Internal Quantum Efficiency Approaching 100%. *Nature Photonics*, 3, 297-303.

[9] Pettersson, L. A. A., Roman, L. S., & Inganas, O. (1999). Modeling photocurrent action spectra of photovoltaic devices based on organic thin films. *J. Appl. Phys*, 86(1), 487-496.

[10] Zhang, C. F., You, H. L., Hao, Y., Lin, Z., & H. and, Zhu. C. X. (2011). Effects of Optical Interference and Annealing on the Performance of Polymer/Fullerene Bulk Heterojunction Solar Cells. *In: Leonid A. Kosyachenko (Ed.) Solar Cells- New Aspects and Solutions, Rijeka: InTech*, 1-26.

[11] Burkhard, G. F., Hoke, E. T., & Mc Gehee, M. D. (2010). Accounting for interference, scattering, and electrode absorption to make accurate internal quantum efficiency measurements in organic and other thin solar cells. *Adv. Mater*, 22(30), 3293-3297.

[12] Hadipour, A., Cheyns, D., Heremans, P., & Rand, B. P. (2011). Electrode considerations for the optical enhancement of organic bulk heterojunction solar cells. *Adv. Energy Mater*, 1(5), 930-935.

[13] Yoshikawa, H., & Adachi, S. (1997). Optical constants of ZnO. *Jpn. J. Appl. Phys*, 36(10), 6237-6243.

[14] Gilot, J., Barbu, I., Wienk, M., & Janssena, R. A. J. (2007). The use of ZnO as optical spacer in polymer solar cells: Theoretical and experimental study. *Appl. Phys. Lett*, 91(11), 113520-1-113520-3.

[15] Ameri, T., Dennler, G., Waldauf, C., Denk, P., Forberich, K., Scharber, M. C., & Hingerl, K. (2010). Realization, characterization, and optical modeling of inverted bulk-heterojunction organic solar cells. *J. Appl. Phys.*, 103(8), 084506-1-084506-6.

[16] Gilot, J., Wienk, M. M., & Janssen, R. A. J. (2010). Optimizing Polymer Tandem Solar Cells. *Adv. Mater*, 22(8), E67-E71.

[17] Ng, A., Li, C. H., Fung, M. K., Djurišić, A. B., Zapien, J. A., Chan, W. K., Cheung, K. Y., Wong, W., & , Y. (2010). Accurate Determination of the Index of Refraction of Polymer Blend Films by Spectroscopic Ellipsometry. *J. Phys. Chem. C*, 114(35), 15094-15101.

[18] Rakić, A. D. (1995). Algorithm for the determination of intrinsic optical constants of metal films: application to aluminum. *Applied Optics*, 34(22), 4755-4767.

[19] Dennler, G., Forberich, K., Ameri, T., Waldauf, C., Denk, P., Brabec, C. J., Hingerl, K., & Heeger, A. J. (2007). Design of efficient organic tandem cells: On the interplay between molecular absorption and layer sequence. *J. Appl.Phys*, 102(12), 123109-1-123109-6.